Journal of Materials Chemistry A

Accepted Manuscript

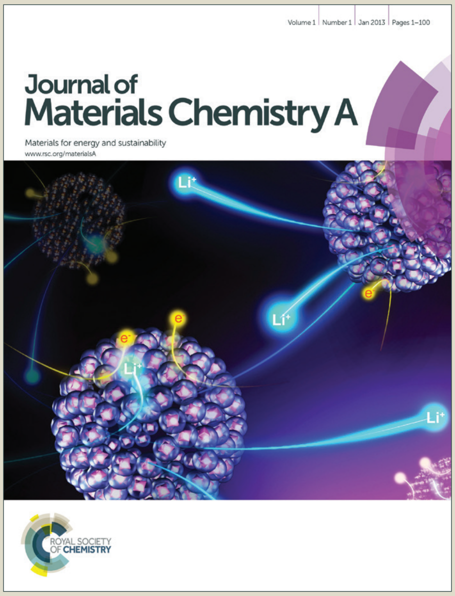

ROYAL SOCIETY OF CHEMISTRY

www.rsc.org/materialsA

Journal of Materials
Chemistry A

Dynamic Article Links ►

Cite this: DOI: 10.1039/c0xx00000x

www.rsc.org/xxxxxx

ARTICLE TYPE

Superior Sodium/Lithium Intercalation and Depressed Moisture Sensitivity of Hierarchical Sandwich-type Nanostructure for Graphene-sulfate Composite: A Case Study on $Na_2Fe(SO_4)_2·2H_2O$

Yu Meng[a], **Sen Zhang***[a] **and Chao Deng***[b]

Received (in XXX, XXX) Xth XXXXXXXXX 20XX, Accepted Xth XXXXXXXXX 20XX
DOI: 10.1039/b000000x

Sulfate-based (SO_4^{2-}) polyanion materials with low cost and ionic-conduction break fresh ground for “rocking-chair” systems. But the high moisture sensitivity and limited conductivity lead to their poor crystal stability and inferior alkaline-ion intercalation chemistry. Here we report a design of graphene-based sandwich-type nanoarchitecture for sulfate. The three-dimensional graphene-based network not only provides continuous electron/ion pathways for fast intercalation kinetics, but also effectively protects crystal structure from deterioration to depress moisture sensitivity. As a case study, the hydrated sulfate ($Na_2Fe(SO_4)_2·2H_2O$)-graphene composite with sandwich-type structure is prepared by a facile low-temperature synthesis. The depressed moisture sensitivity of hierarchical graphene-$Na_2Fe(SO_4)_2·2H_2O$ than pristine one is demonstrated by comparing their hydration process, and moreover, a shell-core hydration mechanism is disclosed. The hierarchical composite exhibits improved electronic conductivity and better sodium/lithium insertion capability than the pristine one. It delivers reversible capacity of 72 and 69 $mAh·g^{-1}$ with redox potentials of 3.415/3.234 V (vs. Na^+/Na) and 3.579/3.483V (vs. Li^+/Li) in sodium and lithium intercalation systems, respectively. Moreover, it also exhibits superior high rate capabilities and good cycling stability, which delivers 81% (for sodium) and 70% (for lithium) of the capacity at the 5 *C* rate. Therefore, the hierarchical sandwich-type architecture is favorable to realizing superior electrochemical performance for the sulfate, which puts a significant step forward to develop low-cost large-scale batteries.

Keyword: sulfate composite; sandwich-type architecture; ion intercalation chemistry; moisture sensitive

1 Introduction

The development of solar and wind energy demands more efficient energy storage systems. Among various options available, electrochemical storage represents the most promising strategy because of its flexibility, high energy conversion efficiency and easy maintenance[1]. Lithium ion battery, which has the highest energy density, is the best choice for portable electronics and electric vehicle[2,3]. However, its application is limited by such disadvantages as high cost and scarce resource of lithium. Therefore, employing other guest ion as an alternative to lithium ion is favorable to developing intercalation chemistry. Sodium ion battery with abundant resource and low cost appears as a promising alternative to lithium ion battery[4,5]. Particularly, the superiority of sodium battery over lithium counterpart becomes more notable as applied in large-scale storage where sustainability and cost are primary concerns. However, the larger ionic radius of sodium than lithium makes it more difficult to find a suitable host for fast ion de/intercalation. Thus it is urgent to discover novel electrode materials with enhanced ion intercalation capability for superior electrochemical properties.

Among present electrode materials, polyanion materials have attracted a large attention. Since 1980s, various polyanionic materials such as silicates (A_2MSiO_4)[6-9], borates ($AMBO_3$)[10], phosphates ($AMPO_4$)[11,12], pyrophosphates (AMP_2O_7)[13-19], and fluorophosphates ($AMPO_4F$)[20,21], have been extensively studied. But the low operating potentials restrict their practical application. Knowing that the redox potential of an intercalation compound is associated with the iono-covalency of metal-anion bonding[22,23], great efforts have been made to search for more electronegative polyanions. On this background, sulfate polyanion (SO_4^{2-}) materials come into sight as a new member in the polyanionic family[24-28]. Compared with other polyanion materials, the sulfates possess stronger electronegativity, which is favorable to achieving higher redox potential. Recently, a series of sulfate-based polyanionic compounds such as $Li_2M(SO_4)_2$[25,26], $LiMSO_4OH$[27,28], $Na_2M(SO_4)_2·nH_2O$[29,30], $Na_2M_2(SO_4)_3$[31] and fluorosulfates of $LiMSO_4F$[32,33] have been investigated. The exploration of these sulfate-based compounds dramatically expands the research scope of intercalation chemistry and provides new opportunities for polyanion materials.

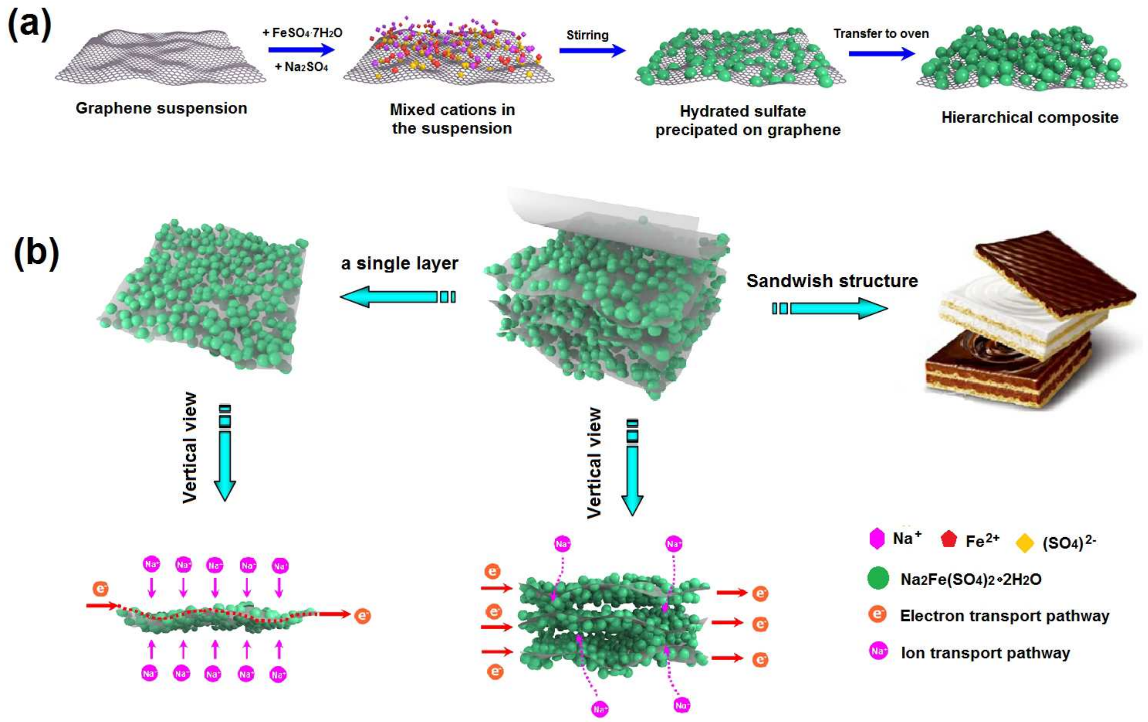

Figure 1(a) Scheme of low-temperature synthetic process for hierarchical $Na_2Fe(SO_4)_2{\cdot}2H_2O$-graphene composite. (b) Schematic illustration of three-dimensional sandwich-type nanostructure for hierarchical $Na_2Fe(SO_4)_2{\cdot}2H_2O$-graphene composite. The vertical view of the hierarchical structure and one enlarged layer with electron/ion transport pathways are illustrated. Cations of Na^+, Fe^{2+}, SO_4^{2-} and the $Na_2Fe(SO_4)_2{\cdot}2H_2O$ particles are indicated by different colors.

Especially, a very recently reported iron-based hydrated sulfate, kröhnkite-type $Na_2Fe(SO_4)_2{\cdot}2H_2O$, has captured our attention. The symmetrical arranged SO_4 tetrahedral and FeO_6 octahedral units construct pseudolayered monoclinic structure for $Na_2Fe(SO_4)_2{\cdot}2H_2O$, which results in the convoluted sodium channels and reversible ion intercalation[30]. As the first member of bihydrated sulfate for sodium ion battery, the discovery of $Na_2Fe(SO_4)_2{\cdot}2H_2O$ opens up new routes for sulfate chemistry. However, facing the same problems as other sulfate-based materials, namely the high moisture sensitivity and limited conductivity[24,25], its crystal structure stability and electrochemical kinetics are severely restricted. Therefore, further improvements on both thermodynamic stability and fast intercalation chemistry are still big challenges for it.

In the "rocking-chair" system, the transports of electron and ion are crucial factors for ion intercalation kinetics. Nanoengineering is an effective strategy to shorten the ion/electron diffusion length and facilitate their transport[34,35]. However, lower volume densities and poor connectivity between individual particles always take place as decreasing particle size. Thus it is highly desirable to discover new strategies to meet ever increasing demands of high power applications. Constructing three-dimensional conductive scaffold is an effective approach to enhance electronic conductivity. The 3D scaffold not only acts as a volume buffer but also builds continuous electron pathways[36-38]. Therefore, if the sulfate nanoparticles could be assembled into a conductive matrix and form hierarchical structure, it would be one of the most effective approaches towards high performance electrode materials.

Following this viewpoint, we design and construct 3D graphene-based sandwich-type architecture for sulfates. We choose bihydrate sulfate ($Na_2Fe(SO_4)_2{\cdot}2H_2O$) as a model material, but this strategy can also be applied to other sulfates as well. A simple low-temperature synthetic approach is employed to prepare the hierarchical composite. As schemed in Figure 1(a), the approach starts from dispersion of graphene nanosheet in distilled water. Then sodium sulfate (Na_2SO_4) and hydrate iron sulfate ($FeSO_4{\cdot}7H_2O$) with desirable amount of iron wire were added to the suspension. After the mixture turns to a uniform sticky suspension, it was transferred to an oven at 70 °C after removal of surplus iron wire for final hierarchical composite. The low-temperature synthesis ensures slowly *in-situ* crystallization of hydrate sulfate, which results in the desirable phase and morphology for the target composite.

Figure 1(b) illustrates the hierarchical sandwich-type nanostructure for the prepared $Na_2Fe(SO_4)_2{\cdot}2H_2O$-graphene composite. The hydrated sulfate nanoparticles uniformly anchored on each graphene nanosheet, and all of graphene-sulfate sheets pile up layer by layer to construct 3D sandwich-type architecture. The graphene-based scaffold provides fast electronic pathways and gives protection for sulfates against structural deterioration. Therefore, such advantages as improved conductivity, better electrochemical kinetics and enhanced structure stability are expected.

Inspired by these advantages, the crystal stability and sodium/lithium intercalation chemistry of prepared sandwich-type $Na_2Fe(SO_4)_2{\cdot}2H_2O$-graphene composite were investigated in this study. The structure deterioration of bihydrate sulfate is discussed and a possible shell-core hydration mechanism is disclosed.

2 Experimental

2.1 Synthesis.

A simple low-temperature synthetic approach is employed to prepare $Na_2Fe(SO_4)_2{\cdot}2H_2O$-graphene hierarchical nanostructures. Graphene was produced by the reduction of graphene oxide prepared by a modified Hummers method, which was purchased from Nanjing XFNANO Materials Tech Co., Ltd. Firstly, the graphene nanosheet was dispersed in 10 ml distilled water under ultrasonic for two hours. Then equal amount of sodium sulfate (Na_2SO_4) and hydrate iron sulfate ($FeSO_4{\cdot}7H_2O$) with desirable amount of iron wires were added to the suspension under magnetic stirring. After it turns to a uniform sticky suspension, the mixture was transferred to an oven at 70 °C with removal of iron wires to final hierarchical sandwich-type $Na_2Fe(SO_4)_2{\cdot}2H_2O$-graphene composite.

2.2 Materials characterization

Powder X-ray diffraction (XRD, Bruker D8/Germany) using Cu Kα radiation was employed to identify the crystalline phase of the material. The experiment was performed by using step mode with a fixed time of 3 s and a step size of 0.02°. The morphology was observed with a scanning electron microscope (SEM, HITACHI S-4700) and a transmission electron microscope (TEM, JEOS-2010 PHILIPS). X-ray photoelectron spectroscopy (XPS, Thermo ESCALAB 250) was employed to measure the chemical state of each element in the surface. Infrared spectra were recorded using a Fourier transform spectrophotometer (FT-IR, Bruker VERTEX 80/Germany). Raman spectra of the composites were collected on a Jobin-Yvon Labor Raman system (Raman, HR-800 HORIBA). The electronic conductivity was measured on the pellet of powder. The powder was pressed into a disk with gold painted on both sides to ensure electrical contact.

2.3 Electrochemical measurements

The electrochemical measurements were carried out using coin type cells. For sodium system, the Na foil was employed as counter and reference electrode and 1 $mol{\cdot}L^{-1}$ $NaClO_4$ dissolved in propylene carbonate (PC) was used as electrolyte. For lithium system, the Li foil was employed as counter and reference electrode and 1 $mol{\cdot}L^{-1}$ $LiPF_6$ dissolved in the mixture of ethylene carbonate (EC) and dimethyl carbonate (DMC) was used as electrolyte. Galvanostatic charge/discharge tests were performed in the potential range of 1.5~4.2 V vs. Na/Na^+ and1.7~4.5 V vs. Li/Li^+ at ambient temperature on a Land battery testing system (Wuhan, China). Current-voltage curves were conducted using a Zivelab electrochemical workstation.

3 Results and Discussion

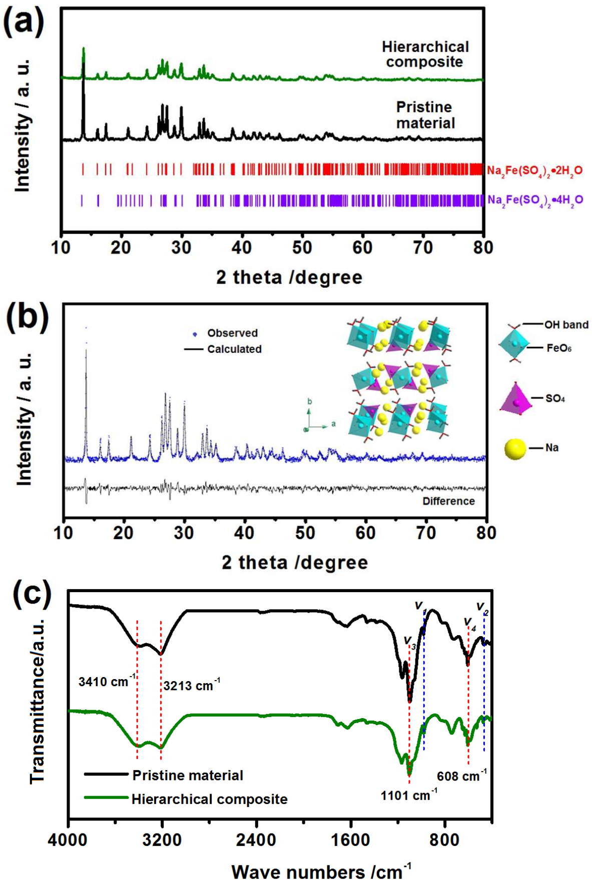

Figure 2 (a) Comparison of XRD patterns between the hierarchical $Na_2Fe(SO_4)_2{\cdot}2H_2O$-graphene composite and pristine $Na_2Fe(SO_4)_2{\cdot}2H_2O$. (b) Rietveld results of pristine sample and the crystal structure of $Na_2Fe(SO_4)_2{\cdot}2H_2O$ is illustrated as inset. (c) FT-IR of the hierarchical and pristine materials.

Figure 2(a) shows XRD patterns of the pristine $Na_2Fe(SO_4)_2{\cdot}2H_2O$ and hierarchical $Na_2Fe(SO_4)_2{\cdot}2H_2O$-graphene composite. Both materials can be indexed to the kröhnkite monoclinic structure (space group: *P2₁/c*) with the parameters of a=5.7685(3), b=12.9835(4), c=5.4536(1) Å, β=105.9623(5)° and a=5.7712(1), b=12.9804(6), c=5.4558(6) Å, β=105.9380(6)° for pristine and hierarchical sample, respectively. Compared with the pristine sample, the hierarchical composite reveals much lower peak densities, which can be attributed to the attachment of sulfate particles to graphene nanosheets. In both materials, the $Na_2Fe(SO_4)_2{\cdot}4H_2O$ phase coexists as a secondary phase as illustrated in Figure 2(b). Based on the Rietveld results, about 3.82% and 3.56% of $Na_2Fe(SO_4)_2{\cdot}4H_2O$ impurity phases were detected in the pristine and hierarchical composite respectively.

The crystal structure of $Na_2Fe(SO_4)_2{\cdot}2H_2O$ are illustrate in inset of Figure 2(b). The $[Fe(SO_4)_2{\cdot}(H_2O)_2]_\infty$ is constructed through each $[FeO_6]$ octahedral sharing four corners with four adjacent $[SO_4]$ tetrahedral and two other corners contribute to structural H_2O molecules. Sodium atoms occupy interstitial positions along the $[Fe(SO_4)_2{\cdot}(H_2O)_2]_\infty$ chains, which in turn

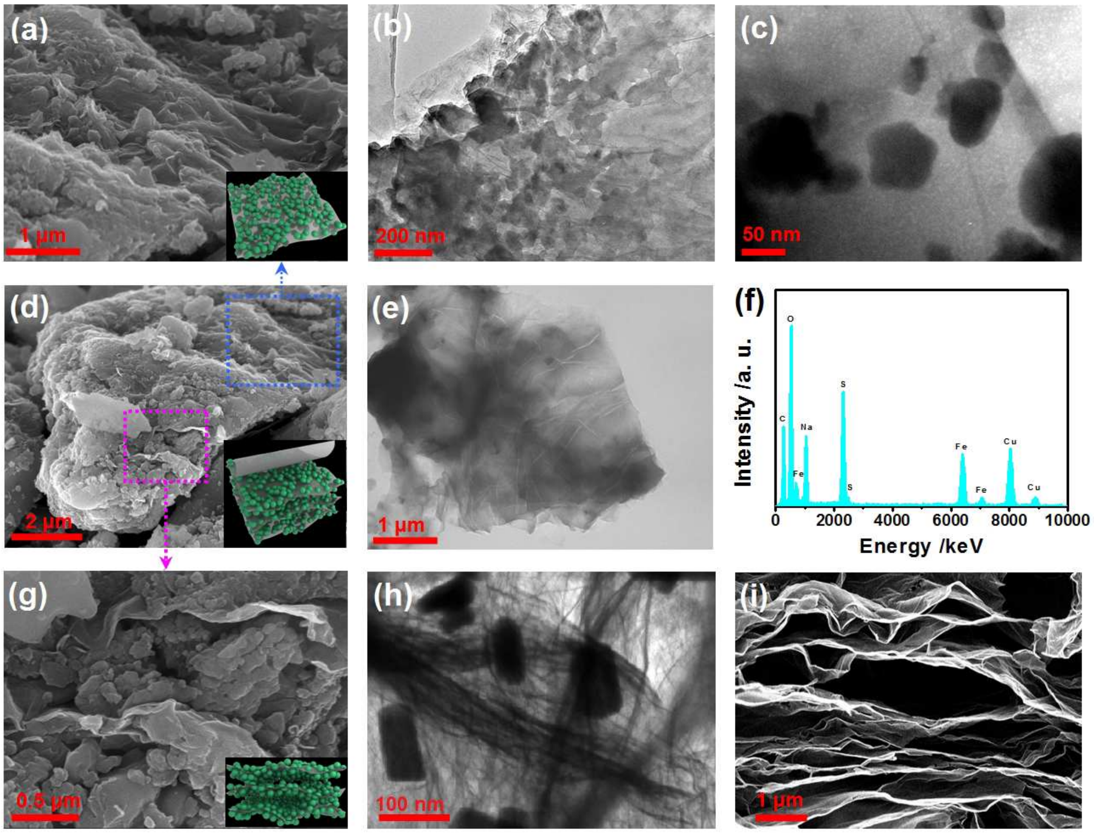

Figure 3 SEM (a, d, e) and TEM (b, c, e, h) images of the hierarchical $Na_2Fe(SO_4)_2{\cdot}2H_2O$-graphene composite and its EDX spectroscopy (f). Images of the whole sandwich-type nanostructure (d and e), one enlarged layer (a, b and c) and vertical view of the hierarchical composite (g and h) are illustrated. The corresponding schematic images are shown as insets of SEM images (a, d and g). The cross-sectional images of pristine graphene network is illustrated in (i).

linked by both Na-O and hydrogen bonds to construct the pseudolayered structure. Sodium ions can diffusion along the well-defined convoluted channels in the framework. Therefore, the structural of $Na_2Fe(SO_4)_2{\cdot}2H_2O$ is favorable to realizing reversible sodium de/intercalation.

In the crystal structure of $Na_2Fe(SO_4)_2{\cdot}2H_2O$, the sulfate units act as the polydentate ligands, which is revealed by FT-IR spectrum. As displayed in Figure 2(c), the spilt of asymmetric stretching (v_3: 1101 cm^{-1}) and bending (v_4: 608 cm^{-1}) mode at low wavenumber indicate the degeneration of pristine peaks for sulfate group. It demonstrates the overall asymmetry of SO_4 arrangement and indicates its connecting role in the crystal structure. On the other hand, obvious broad peaks at 3213 and 3410 cm^{-1} are observed in the high wavenumber, which corresponds to the hydroxyl groups and H_2O units. It further confirms the enriching hydroxyl groups in the crystal structure. Compared with the pristine one, the hierarchical composite displays much lower intensities in the low wavenumber (400~1700 cm^{-1}), which indicates the dramatically decreased signal of sulfate group in the sandwich-type architecture.

Raman spectra were further employed to characterize the carbon matrix in the hierarchical composite (Figure S1). Two characteristic signatures located at 1357 and 1589 cm^{-1} were observed for the hierarchical composite, corresponding to the *D* (disordered carbon) and *G* (graphene carbon) bands[39]. The high intensity of *G* band and low value of the *D/G* intensity ratio demonstrate its high sp^2 domain size. Therefore, all of the above results confirm that the $Na_2Fe(SO_4)_2{\cdot}2H_2O$-graphene composite with desirable crystal structure has been synthesized via present low-temperature strategy.

The morphology and microstructure of the hierarchical composite were investigated by SEM and TEM observations. As shown in Figure 3(d) and (e), the sulfate nanoparticles are encompassed by graphene sheets, which results in the hierarchical architecture of the composite. The enlarged parallel view of one layer (Figure 3a~c) demonstrates that the nanoparticles with the diameter of 50-100 nm are well wrapped by large graphene sheet and results in each layer with hierarchical structure. The vertical view of graphene network (Figure 3i) reveals that the graphene sheets pile up layer by layer to construct 3D conductive framework for stacking sulfate nanoparticles. It provides intimate contact between each other and builds continuous electron transport pathways. The vertical view of the hierarchical composite (Figure 3g and h) further indicates that the nanoparticles are anchored on each graphene sheet on both sides, which forms the sandwich-type architecture of the composite. Moreover, the EDX result (Figure 3f) suggests that the element ratio of Na: Fe: S for the hierarchical composite is 1.965:1: 2.042, which is coincided with the designed value. Therefore, the results demonstrate that the $Na_2Fe(SO_4)_2·2H_2O$-graphene composite with hierarchical sandwich-type nanostructure has been successfully constructed.

In order to investigate the effects of hierarchial sandwich nanostructure on electronic transport capability for sulfates, the electronic conductivity of hierarchical $Na_2Fe(SO_4)_2·2H_2O$-graphene composite and pristine $Na_2Fe(SO_4)_2·2H_2O$ are estimated at room temperature. As displayed in Figure 4(a), the linear fits of the current-voltage curves were reached for both materials. The calculated electronic conductivity (σ) for the pristine $Na_2Fe(SO_4)_2·2H_2O$ is about $9.4×10^{-15}$ $s·cm^{-1}$ at ambient temperature (Figure 2b). The result is in agreement with the previously reported sulfates such as $Li_2Fe(SO_4)_2$ ($σ\sim10^{-16}$ $s·cm^{-1}$)[26] and $Li_2Co(SO_4)_2$ (monoclinic phase, $σ\sim10^{-18}$ $s·cm^{-1}$; orthorhombic phase, $σ\sim10^{-14}$ $s·cm^{-1}$)[25]. All these electronic conductivity values of the sulfates were much lower than the other polyanion materials, for example, the most commonly $LiFePO_4$[40]: $σ\sim10^{-9}$ $s·cm^{-1}$. Thus the poor conductivity has become one of the most serious problems for sulfates as electrode materials. Significant improvement was observed for the hierarchical composite, which increased to about $4.33×10^{-4}$ $s·cm^{-1}$ at room temperature. The enhanced conductivity is associated with the special architecture of hierarchical composite. The graphene-based skeleton constructs 3D conductive network for sulfates and the sandwich-type structure ensures the intimate contact between nanoparticles and the conductive network. Both facilitate electron transport and result in the good conductivity. Thus the results confirm that graphene-based sandwich hierarchical nanostructure is high-efficient to modify poor electronic conductivity for sulfate-based materials.

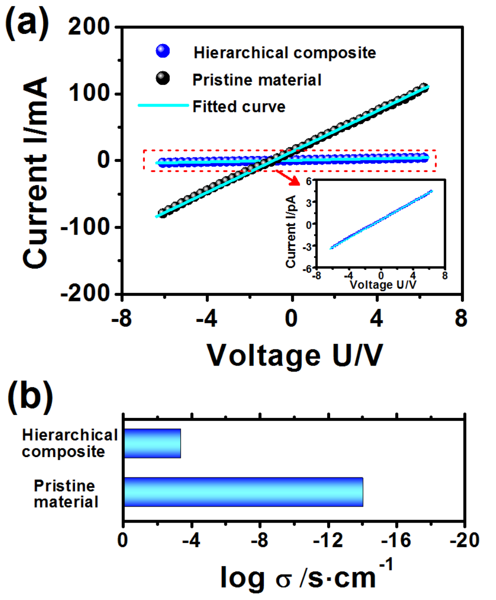

Figure 4 (a) Current-voltage response of the hierarchical $Na_2Fe(SO_4)_2·2H_2O$-graphene composite and pristine $Na_2Fe(SO_4)_2·2H_2O$ for the determination of electronic conductivity at room temperature. (b) Comparison of electronic conductivities between the hierarchical composite and the pristine one.

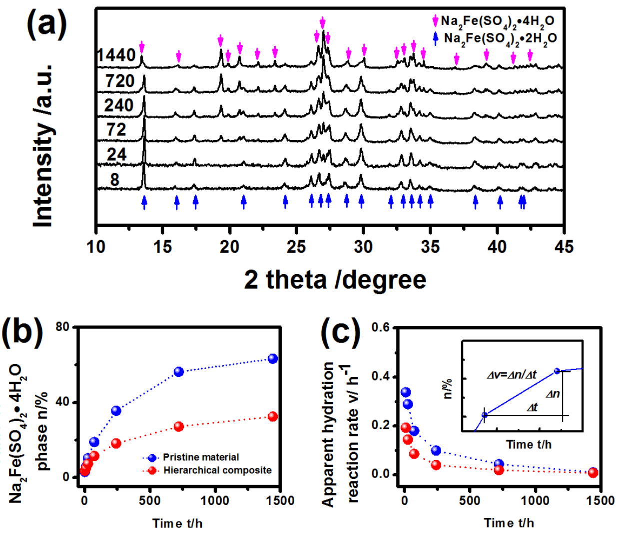

Figure 5 (a) XRD patterns of pristine $Na_2Fe(SO_4)_2·2H_2O$ exposed to air for different time; (b) the change of ratio of $Na_2Fe(SO_4)_2·4H_2O$ phase in the pristine material and hierarchical composite during air-exposure; (c) The relationship between the calculated apparent reaction rates and exposure time for both materials. A typical example for the calculation of apparent reaction rate is shown as an inset.

The high moisture sensitivity is another special character for sulfate-based compounds. It leads to easy structure deterioration during storage and restricts their practical application. This problem is even serious for the bihydrate sulfate ($Na_2Fe(SO_4)_2·2H_2O$). In order to investigate the effects of sandwich-type architecture on the moisture sensitivity of sulfates, we expose both the pristine and hierarchical samples to ambient environment and compare their XRD patterns after different exposure time (Figure 5a). Based on the refinement results of XRD patterns, the ratios of $Na_2Fe(SO_4)_2·2H_2O$ and $Na_2Fe(SO_4)_2·4H_2O$ phases in both samples are determined. As displayed in Figure 5(b), the ratio of $Na_2Fe(SO_4)_2·4H_2O$ impurity phase in both samples initially dramatically increases as increasing exposure time. Then it turns to slow down and finally becomes stable after two months. The result indicates that the structural deterioration of bihydrate sulfate is associated with the hydration reaction. Compared with the pristine material, less structure deterioration was observed for the hierarchical composite. After one month's air-exposure, the ratio of $Na_2Fe(SO_4)_2·4H_2O$ phase in the hierarchical sample is only half of the value for the pristine sample. Even after two months, there is still about two thirds of the original $Na_2Fe(SO_4)_2·2H_2O$ phase in the hierarchical composite. The results demonstrate that the hierarchical composite has higher ratio of $Na_2Fe(SO_4)_2·2H_2O$ phase than pristine one under same exposure-time, which demonstrates its improved structure stability and depressed moisture sensitivity.

In order to investigate the process of hydration reaction, an apparent oxidation rate is calculated as following equation:

$$dv=dm/dt \qquad (1)$$

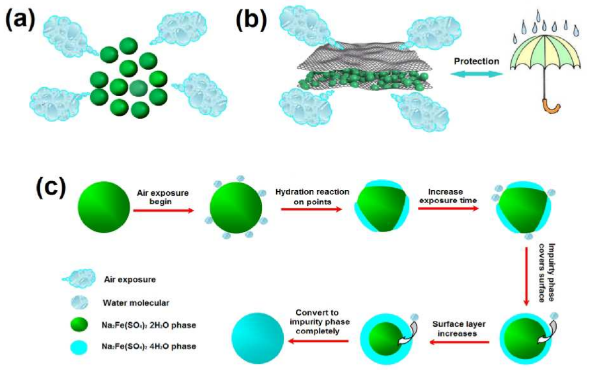

Figure 6 Scheme of (a) pristine $Na_2Fe(SO_4)_2·2H_2O$ and (b) the hierarchical sandwich-type $Na_2Fe(SO_4)_2·2H_2O$-graphene composite during air-exposure. (c) Schematic illustration of the shell-core hydration process for $Na_2Fe(SO_4)_2·2H_2O$ during air-exposure.

where *v* is the apparent hydration rate; *m* is the mole ratio of hydrated phase; *t* is the air exposure time.

The calculation results are summarized in Figure 5(c) and a typical example calculation is displayed as an inset. For both samples, apparent hydration rate initially decreases quickly as air-exposure time increases. Then it turns to slow and finally become stable. Compared with pristine sample, the hierarchical one exhibits much lower hydration rates. On the other hand, the O1s XPS spectra of pristine sample suggests the area of peaks corresponding to H_2O and OH^- after air-exposure are much higher than those of unexposure one (Figure S2). It indicates that the contents of H_2O and OH^- on the particle surface increase during air-exposure. Therefore, both apparent reaction rate and XPS spectra results suggest that the product of hydrated reaction initially exists on the surface of the particle, which would embarrass the hydration reaction to inner part of particle and leads to decreased reaction rate as increasing time.

The above results suggest a shell-core hydration mechanism which is depicted in Figure 6(a) and (c). When the sulfate particle is exposed in the moisture-bearing air, water is absorbed on the surface of the particle and the hydration reaction thus takes place. Initially, the hydrated sulfate ($Na_2Fe(SO_4)_2·4H_2O$) scatters randomly on the surface of the particle of $Na_2Fe(SO_4)_2·2H_2O$. The surface occupied by the hydrated sulfate grows continuously until the entire outer surface is covered by the hydrated phase. The hydration rate in this process is proportional to the unhydrated surface area which continually decreases with the progression of the hydration reaction. When an outer “shell” of the hydrated phase is formed, the absorbed water molecules have to penetrate through the “shell” in order to reach the inner “core” of the sulfate, thus the hydration rate dramatically slows down upon further air exposure. The hydration rate in this stage is inversely proportional to the thickness of the “shell”. Therefore, the variation of the hydration rate predicated by the shell-core hydration mechanism is in accordance with that observed by the experimental measurements while the air exposure of the pristine sample is involved. This is an indication of the validity of the core-shell hydration mechanism.

For the hierarchical composite, the graphene nanosheet wrapped the sulfate particles, which decreases the opportunities of direct contact between the particle and water molecule (Figure 6b). Thus the sandwich-type structure effectively embarrasses the hydration reaction of sulfate particles, which results in the decreased apparent reaction rate. Therefore, the hierarchical composite exhibits better crystal structure stability, less moisture sensitivity and easier storage than the pristine one. Combined all of the above results, it indicates that the hierarchical sandwich-type nanoarchitecture is favorable to enhancing the electronic conductivity and suppressing the moisture sensitivity of the sulfate.

Inspired by the advantages of hierarchical sandwich-type architecture, the sodium and lithium ion intercalation chemistry of hierarchical $Na_2Fe(SO_4)_2·2H_2O$-graphene composite was investigated. Figure 7 (a) and (b) shows the galvanostatic charge-discharge characteristics of the hierarchical composite in sodium and lithium systems, respectively. It exhibits electrochemical activities in both systems. For sodium intercalation system (Figure 7a), the composite exhibits an initially discharge capacity of 72 $mAh·g^{-1}$ at 0.05 *C* rate. One pair of charge and discharge potential plateaus is observed in the galvanostatic charge/discharge profiles, corresponding well to the oxidation (3.415 V vs. Na^+/Na) and reduction (3.234 V vs. Na^+/Na) peaks in the dQ/dV curve. The symmetrical redox potentials indicate the reversible redox reaction of Fe^{2+}/Fe^{3+} in the hydrate sulfate ($Na_2Fe(SO_4)_2·2H_2O$), which agree well with those reported by Barpanda et al[30]. The shape of galvanostatic curves changes slightly during cycles and it turns to stable after five to ten cycles.

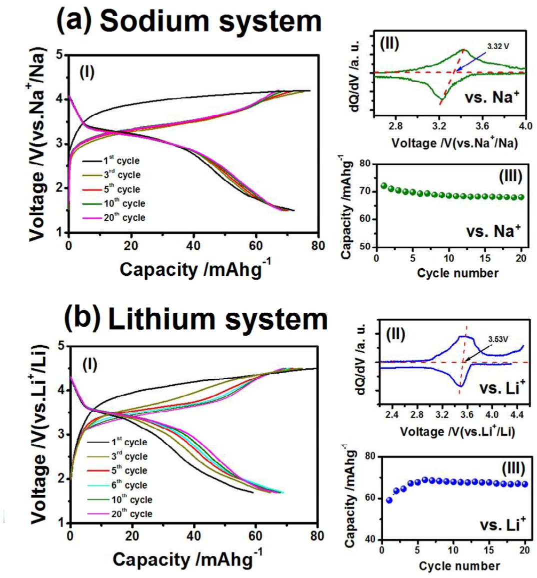

Figure 7 Galvanostatic charge-discharge characteristics of hierarchical $Na_2Fe(SO_4)_2·2H_2O$-graphene composite in (a) sodium and (b) lithium intercalation systems. The charge/discharge profiles of 1, 3, 5, 10 and 20 cycles (i), typical dQ/dV curve (ii) and cycling properties (iii) are displayed.

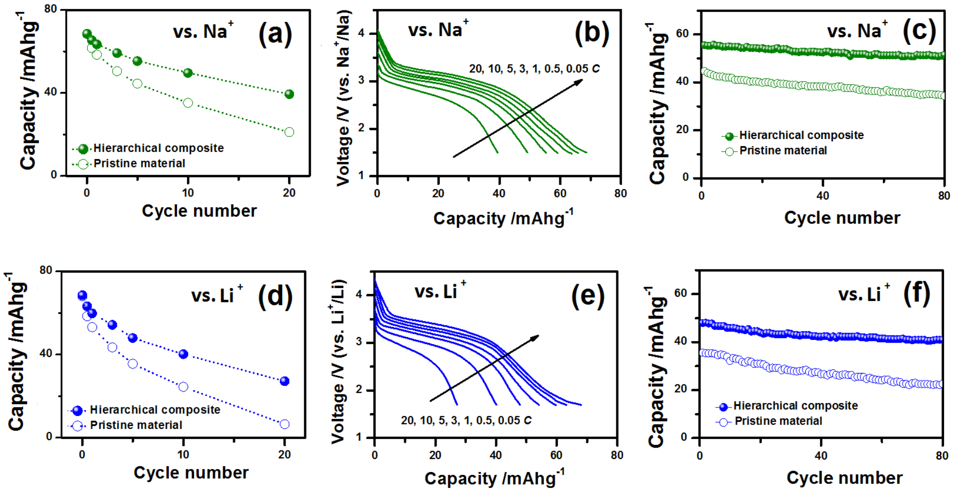

Figure 8 Comparison of rate capability between the hierarchical $Na_2Fe(SO_4)_2{\cdot}2H_2O$-graphene composite and pristine $Na_2Fe(SO_4)_2{\cdot}2H_2O$ in sodium (a) and lithium (d) systems. The galvanostatic discharge curves of the hierarchical composite at different current densities in sodium (b) and lithium (e) systems. Long-term cycling properties of the hierarchical composite and pristine material at 5*C* rate in sodium (c) and (f) lithium systems.

Compared with the sodium system, the electrochemical behaviors of the sulfates in lithium intercalation system are different. As displayed in Figure 7 (b), it exhibits only a low discharge capacity of 59 mAh·g^{-1} in the first cycle with short and inconspicuous potential plateau. As increases cycle number, both the discharge capacities and potential plateau gradually increase. After six cycles, the capacity reach the maximum value of 69 mAh·g^{-1}. Then it turns to stable and slightly decreases in the following cycles. The change of charge/discharge characteristics in lithium system is associated with the structure altering process of hybrid ion systems. Barker[41], Nazar[42] and Banks[43,44] et al have operated the sodium intercalated materials such as $Na_3V_2(PO_4)_2F_3$, $Na_3V_2(PO_4)_3$ and $NaVPO_4F$ in a lithium based electrolyte and discovered hybrid ion batteries (HIB). Based on the rocking chair chemistry of HIB, the gradual capacity alteration process during initial cycles is associated with the initially temporary disorder induced by hybrid de/insertion process, which would be suppressed and reformed by the predominately Li ion transport in the sequential cycles due to a vast excess of Li[41-44]. And the stabilization suggests the completion of the transformation process. Therefore, the change of charge/discharge profiles in our study can be attributed to the transformation process from the hybrid ions (sodium and lithium) transport to the lithium dominates transport. Evidences from the *ex-situ* XRD patterns also support this intercalation process. As displayed in Figure S3, obvious right shift was observed in the XRD patterns after initial cycle, which suggests the alteration of crystal volume during initial cycle. Then the shift turns to slow and become stable after five cycles. It suggests the structure re-construction process takes place during initial a few cycles and completes after five cycles. The *ex-situ* XRD results coincide well with the capacity change during cycles. Two well defined charge/discharge potential plateaus were observed in the charge/discharge profile after stabilization, which corresponds to the oxidation (3.579 V vs. Li^+/Li) and reduction (3.483 V vs. Li^+/Li) peaks in the dQ/dV curve. The redox potential in lithium system is higher than that in sodium system, which can be attributed to the different redox potentials of two alkaline metals. Therefore, all of above results demonstrate that the $Na_2Fe(SO_4)_2{\cdot}2H_2O$ composite can be employed as the host material for Li as well as Na.

Motivated by the good compatibilities of Na/Li ion, the high rate capability and cycling stability of both pristine and the hierarchical samples in sodium/lithium ion batteries were investigated. A series of current densities, from 0.05 *C* to 10 *C* are employed to evaluate the rate capability. All of the rate capacity tests were carried out after five to ten precycles to eliminate initial instability. As displayed in Figure 8 (a) and (d), in both lithium/sodium intercalation systems, similar capacities are observed for the pristine and hierarchical composites at 0.05 *C* rate. When the current density is high than 0.5 *C*, obvious higher capacity was observed for the hierarchical composite than the pristine one. As the current densities increases, the differences between two samples become more significant. For example, the hierarchical composite delivers 63.5 and 49.6 mAh·g^{-1} of the capacities at the 1 *C* and 10 *C* rates in sodium battery. They are higher than those of the pristine material, which only delivers 58.4 and 35.2 mAh·g^{-1} of capacities at 1 *C* and 10 *C*, respectively. Moreover, both materials exhibits better properties in sodium ion system than those in lithium ion system, especially at high rate (Figure 8b and e). For example, the hierarchical composite exhibits the capacity of 55.3 and 39.4 mAh·g^{-1} in the sodium ion battery at 5 *C* and 20 *C* rate, corresponding 81% and 57% of the capacity at 0.05 *C*. The values are higher than those in lithium ion battery, which are 47.9 and 27.1 mAh·g^{-1} at 5 *C* and 20 *C* corresponding to only 70% and 40% of capacity at 0.05 *C*. The inferior property of sodium-containing materials in lithium ion system have also been observed in previous reports on $Na_3V_2(PO_4)_3$, $NaCo(PO_4)_2P_2O_7$, $Na_7V_4(P_2O_7)_4(PO_4)$, et al[41-44]. It is proposed to be associated with the structure change induced by higher charge density of lithium ion, which worsens the high rate capability of the composite.

On the other hand, the hierarchical composite also exhibit better cycling property than the pristine one (Figure 8c and f). At the 5 *C* rate, higher cycling stability of 92% and 85% are obtained for the hierarchical composite in sodium and lithium system respectively, which are higher than those of the pristine one (77% for sodium and 63% for lithium system). On the basis of above results, the superb high rate property and good cycling stability of graphene-sulfate composite can be attributed to the advantages of the hierarchical sandwich-type architecture as illustrated in Figure 1. The 3D graphene-based framework constructs conductive network for the sulfates, which provides continuous electron/ion pathway and guarantees the effective electron contact upon prolonged cycling. Therefore, it is favorable to the fast electrochemical kinetics and stable cycling property.

4 Conclusions

In summary, a graphene-based sandwich-type structure has been designed and fabricated to develop high-performance sulfate-based electrode materials. The hierarchical nanoarchitecture consisting of 3D graphene network and sulfate nanoparticles effectively addresses the inherent problems such as intrinsically low electronic conductivity and high moisture sensitivity in the sulfate chemistry. As a case study, the hierarchical graphene-$Na_2Fe(SO_4)_2 \cdot 2H_2O$ composite was constructed. It exhibits good sodium/lithium insertion capability, superior high rate property and depressed moisture sensitivity. The improved properties are attributed to 3D conductive framework and hierarchical sandwich architecture, which provide continuous electronic pathways for fast kinetics and gives strong protection for sulfates against structure deterioration. Therefore, the graphene-based hierarchical sandwich-type architecture is demonstrated to be a promising approach for sulfate-based materials, in view of wide validity, superior electrochemical performance and easy storage.

Acknowledgement

This work is supported by the National Natural Science Foundation of China (No. 21001036, 50902041), Program for New Century Excellent Talents in Heilongjiang Provincial University (No. 1253-NCET-012) and Natural Science Foundation of Heilongjiang Province (No. QC2013C008).

Notes and references

[a] *Key Laboratory of Superlight Material and Surface Technology, Ministry of Education, College of Materials Science and Chemical Engineering, Harbin Engineering University, Harbin 150001, Heilongjiang, China; E-Mail: senzhang@hrbeu.edu.cn*
[b] *Key Laboratory for Photonic and Electronic Bandgap Materials, Ministry of Education; College of Chemistry and Chemical Engineering, Harbin Normal University, Harbin, 150025, Heilongjiang, China; E-Mail: chaodenghsd@sina.com*

† Electronic Supplementary Information (ESI) available: Raman spectra of hierarchical composite, O1s XPS spectra of pristine hydrate phase under different exposure time and ex-situ XRD patterns after different cycles in lithium intercalation system. See DOI: 10.1039/b000000x/

1 A. Tamada, *MRS Bulletin* **2014**, *39*, 423.
2 J. B. Goodenough, K. S. Park, *J. Am. Chem. Soc.* **2013**, *135*, 1167.
3 J. M. Tarascon, M. Armand, *Nature* **2001**, *414*, 359.
4 V. Palomares, P. Serras, I. Villaluenga, K. B. Hueso, J. C. Gonzalez, T. Rojo, *Energy Environ. Sci.* **2012**, *5*, 5884.
5 K. Kubota, N. Yabuuchi, H. Yoshida, M. Dahbi, S. Komaba, *MRS Bulletin*. **2014**, *39*, 416.
6 M. S. Islam, R. Dominko, C. Masquelier, C. Sirisopanaporn, A. R. Armstrong, P. G. Bruce, *J. Mater. Chem.* **2011**, *21*, 9811.
7 C. Deng, S. Zhang, S. Y. Yang, *Mater. Chem. Phys.* **2010**, *120*, 14.
8 R. Dominko, M. Gaberscek, A. Meden, M. Remskar, J. Jamnik, *Electrochem. Commun.* **2006**, *8*, 217.
9 C. Deng, S. Zhang, S. Y. Yang, B. L. Fu, L. Ma, *J. Power Sources* **2011**, *196*, 386.
10 L. Tao, G. Rousse, J. N. Chotard, L. Dupont, S. Bruyere, D. Hanzel, G. Mali, R. Dominkok, S. Levasseur, C. Masquelier, *J. Mater. Chem. A* **2014**, *2*, 2060.
11 A. K. Padhi, K. S. Nanjundaswamy, C. Masquelier, J. B. Goodenough, *J. Electrochem. Soc.* **1997**, *144*, 2581.
12 A. K. Padhi, V. Manivannan, J. B. Goodenough, *J. Electrochem. Soc.* **1998**, *145*, 1518.
13 S. Nishimura, M. Nakamura, R. Natsui, A. Yamada, *J. Am. Chem. Soc.* **2010**, *132*, 13596.
14 T. Ye, P. Barpanda, S. Nishimura, N. Furtuta, S. C. Chung, A. Yamada, *Chem. Mater.* **2013**, *25*, 3623.
15 L. Tan, S. Zhang, C. Deng, *J. Power Sources* **2015**, *275*, 6.
16 P. Barpanda, S. Nishimura, A. Yamada, *Adv. Energy Mater.* **2012**, *2*, 841.
17 P. Barpanda, T. Ye, S. Nishimura, S. Chung, Y. Yamada, M. Okubo, H. Zhou, A. Yamada, *Electrochem. Commun.* **2012**, *24*, 116.
18 P. Barpanda, T. Ye, M. Avdeev, S. Chung, A. Yamada, *J. Mater. Chem. A* **2013**, *1*, 4194.
19 P. Barpanda, G. Liu, C. D. Ling, M. Tamaru, M. Avdeev, S. Chung, Y. Yamada, A. Yamada, *Chem. Mater.* **2013**, *25*, 3480.
20 M. Prabu, M. V. Reddy, S. Selvasekarapandian, G. V. S. Rao, B. V. R. Chowdari, *Electrochim. Acta* **2012**, *85*, 572.
21 B. L. Ellis, T. N. Ramesh, W. N. Rowan-weetaluktuk, D. H. Ryan, L. F. Nazar, *J. Mater. Chem.* **2012**, *22*, 4759.
22 B. C. Melot, D. O. Scanlon, M. Reynaud, G. Rousse, J. N. Chotard, M. Henry, J. M. Tarascon, *ACS Appl. Mater. Interfaces* **2014**, *6* 10832.
23 G. Hautier, A. Jain, H. Chen, C. Moore, S. P. Ong, G. Ceder, *J. Mater. Chem.* **2011**, *21*, 17147.
24 G. Rousse, J. M. Tarascon, *Chem. Mater.* **2014**, *26*, 394.
25 L. Lander, M. Reynaud, G. Rousse, M. T. Sougrati, C. L. Robert, R. J. Messinger, M. Deschamps, J. M. Tarascon, *Chem. Mater.* **2014**, *26*, 4178.
26 J. M. Clark, C. Eames, M. Reynaud, G. Rousse, J. N. Chotard, J. M. Tarascon, M. S. Islam, *J. Mater. Chem. A* **2014**, *2*, 7446.

27 C. V. Subban, M. Ati, G. Rousse, A. M. Abakumov, G. V. Tendeloo, R. Janot, J. M. Tarascon, *J. Am. Chem. Soc.* **2013**, *135*, 3653.

28 C. Eames, J. M. Clark, G. Rousse, J. M. Tarascon, M. S. Islam, *Chem. Mater*. **2014**, *26*, 3672.

29 M. Reynaud, G. Rousse, A. M. Abakumov, M. T. Sougrati, G. V. Tendeloo, J. N. Chotard, J. M. Tarascon, *J. Mater. Chem. A* **2014**, *2*, 2671.

30 P. Barpanda, G. Oyama, C. D. Ling, A. Yamada, *Chem. Mater.* **2014**, *26*, 1297.

31 P. Barpanda, G. Oyama, S. I. Nishimura, S. C. Chung, A. Yamada, *Nature Commu.* **2014**, *5*, 4358.

32 N. Recham, J. N. Chotard, L. Dupont, C. Delacourt, W. Walker, M. Armand, J. M. Tarascon, *Nature Mater.* **2010**, *9*, 68.

33 P. Barpanda, M. Ati, B. C. Melot, G. Rousse, J. N. Chotard, M. L. Doublet, M. T. Sougrati, S. A. Corr, J. C. Jumas, J. M. Tarascon, *Nature Mater*. **2011**, *10*, 772.

34 J. Maier. *Nature Mater*. **2005**, *4*, 805.

35 P. G. Bruce, B. Sctrosati, J. M. Tarascon, *Angew. Chem. Int. Ed.* **2008**, *47*, 2930-2946.

36 S. Xin, Y. G. Guo, L. J. Wan, *Accounts Chem. Res.* **2012**, *45*, 1759.

37 S. Li, Y. F. Dong, L. Xu, X. Xu, L. He, L. Q. Mai, *Adv. Mater*. **2014**, *26*, 3545.

38 S. H. Lee, V. Sridhar, J. H. Jung, K. Karthikeyan, Y. S. Lee, R. Mukherjee, N. Koratkar, I. K. Oh, *ACS Nano* **2013**, *7*, 4242.

39 L. Fei, Q. L. Lin, B. Yuan, G. Chen, P. Xie, Y. L. Li, Y. Xu, S. G. Deng, S. Smirnov, H. M. Luo, *ACS Appl. Mater. Interfaces* **2013**, *5* 5330.

40 P. S. Herle, B. Ellis, N. Coombs, L. F. Narzar, *Nature Mater*. **2004**, *3*, 147.

41 J. Barker, R. K. B. Gover, P. Burns, A. J. Bryan, *J. Electrochem. Soc.* **2007**, *153*, A882.

42 B. L. Ellis, W. R. M. Makahnouk, Y. Makimura, K. Toghill, L. F. Nazar, *Nature Mater*. **2007**, *6*, 749.

43 W. X. Song, X. B. Ji, Y. P. Yao, H. J. Zhu, Q. Y. Chen, Q. Q. Sun, C. E. Banks. *Phys. Chem. Chem. Phys.* **2014**, *16*, 3055.

44 W. X. Song, X. B. Ji, Z. P. Wu, Y. R. Zhu, Y. P. Yao, L. K. Huangfu, Q. Y. Chen, C. E. Banks. *J. Mater. Chem. A* **2014**, *2*, 2517.